Acta Materialia 132 (2017) 389–394

Contents lists available at ScienceDirect

Acta Materialia

journal homepage: www.elsevier.com/locate/actamat

Full length article

Multiscale measurements on temperature-dependent deformation of a textured magnesium alloy with synchrotron x-ray imaging and diffraction

L. Lu [a, b, c], B.X. Bie [c], Q.H. Li [b], T. Sun [d], K. Fezzaa [d], X.L. Gong [a, **], S.N. Luo [b, c, *]

[a] CAS Key Laboratory of Mechanical Behavior and Design of Materials, Department of Modern Mechanics, University of Science and Technology of China, Hefei, Anhui 230027, PR China
[b] Key Laboratory of Advanced Technologies of Materials, Ministry of Education, Southwest Jiaotong University, Chengdu, Sichuan 610031, PR China
[c] The Peac Institute of Multiscale Sciences, Chengdu, Sichuan 610031, PR China
[d] Advanced Photon Source, Argonne National Laboratory, Argonne, IL 60439, USA

ARTICLE INFO

Article history:
Received 17 March 2017
Received in revised form
26 April 2017
Accepted 27 April 2017
Available online 29 April 2017

Keywords:
Multiscale measurements
Digital image correlation
X-ray diffraction
Temperature
Twinning

ABSTRACT

In situ synchrotron x-ray imaging and diffraction are used to investigate deformation of a rolled magnesium alloy under uniaxial compression at room and elevated temperatures along two different directions. The loading axis (LA) is either perpendicular or parallel to the normal direction, and these two cases are referred to as LA⊥⟨*c*⟩ and LA∥⟨*c*⟩ loading, respectively. Multiscale measurements including stress–strain curves (macroscale), strain fields (mesoscale), and diffraction patterns (microscale) are obtained simultaneously. Due to initial texture, $\{10\bar{1}2\}$ extension twinning is predominant in the LA⊥⟨*c*⟩ loading, while dislocation motion prevails in the LA∥⟨*c*⟩ loading. With increasing temperature, fewer $\{10\bar{1}2\}$ extension twins are activated in the LA⊥⟨*c*⟩ samples, giving rise to reduced strain homogenization, while pyramidal ⟨*c* + *a*⟩ slip becomes readily activated, leading to more homogeneous deformation for the LA∥⟨*c*⟩ loading. The difference in the strain hardening rates is attributed to that in strain field homogenization for these two loading directions.

1. Introduction

Magnesium has a hexagonal close-packed structure. Easy glide basal ⟨*a*⟩ systems [1], in addition to prismatic and pyramidal ⟨*a*⟩ slips which require higher driving forces and/or elevated temperatures for activation [2,3], are incapable of accommodating any plastic strain along the crystallographic *c*-axis. Pyramidal ⟨*c* + *a*⟩ slip is generally assumed to provide the additional degree of freedom needed for an arbitrary plastic strain, as confirmed by experiments [2,4–6]. Alternatively, extension twinning [7–10] can also allow the *c*-axis strain component required for generalized deformation. Given these deformation modes, plastic deformation of magnesium and its alloys is strongly affected by textures and temperature due to slip, twinning and their interactions. Recently, deformation of magnesium alloy across multiple temporal and spatial scales was characterized at room temperature, and such measurements allow one to make concrete connections between different length scales, particularly meso- and microscales.

The occurrence of strain localizations near the yield point is directly related to twin nucleation and growth, as verified by *ex situ* electron back-scatter diffraction (EBSD) [11]. Uniaxial tensile tests on Mg alloy sheets with optical digital image correlation (DIC) and EBSD techniques revealed that large strain gradients develop on the sheet surface parallel and perpendicular to the loading direction, while little deformation occurs in the thickness direction [12]. The complex strain fields that emerge at the onset of extensive deformation twinning in Mg alloy was also investigated with optical DIC, and ±45° strain localizations were monitored at length scales from grains to the sample scale [13]. Synchrotron-based multiscale measurements were established to investigate anisotropic deformation of Mg alloy at room temperature: extension twinning (microscale) induces homogenized strain fields (mesoscale) which in turn lead to increase in strain hardening rate (macroscale) [14].

* Corresponding author. Key Laboratory of Advanced Technologies of Materials, Ministry of Education, Southwest Jiaotong University, Chengdu, Sichuan 610031, PR China.
** Corresponding author.
E-mail addresses: gongxl@ustc.edu.cn (X.L. Gong), sluo@pims.ac.cn, sluo@swjtu.cn (S.N. Luo).

http://dx.doi.org/10.1016/j.actamat.2017.04.065
1359-6454/

As a structural material, Mg alloys exhibit poor formability at room temperature, and a usual approach to overcoming this drawback is to form the material at an elevated temperature [15,16]. Wide applications of Mg alloys require a better understanding of deformation mechanisms at elevated temperatures. A working model [17] was developed to incorporate the temperature dependence of deformation twinning as regards mechanical behavior of Mg alloy sheets. It is found that there is a greater availability of slip planes as the critical resolved shear stress (CRSS) of different slip systems decrease with increasing temperature, effectively increasing the formability of the material [17]. Moreover, the effects of the strain paths [18] and strain rates [18] on deformation of Mg alloys at different temperatures were examined. Extension twinning and basal slip are weakly temperature-dependent, but for compression twinning, and prismatic and pyramidal $\langle c+a\rangle$ slips, CRSS decreases substantially with increasing temperature [19]. As mentioned above, multiscale measurements based on optical or x-ray techniques were used to investigate deformation of Mg alloys at room temperature. However, simultaneous, *in situ*, real-time, multiscale, measurements at elevated temperatures are still lacking.

In this work, uniaxial compression experiments are conducted to investigate the effects of texture and temperature on mechanical behavior of an rolled magnesium alloy AZ31, using *in situ* synchrotron x-ray diffraction and imaging. Multiscale measurements on macroscale stress–strain curves, mesoscale strain fields, and microstructure evolution are obtained simultaneously at room and elevated temperatures. Such measurements reveal anisotropy in its deformation across different spatial scales, and allow us to make connections between them. In particular, fewer $\{10\bar{1}2\}$ extension twins are activated with increasing temperature, and result in reduced strain homogenization, while readily activated pyramidal $\langle c+a\rangle$ slip leads to more homogeneous deformation.

2. Materials and experiments

A commercial rolled AZ31 magnesium alloy sheet (3 wt% Al, 1 wt % Zn, and balance Mg) is used for uniaxial compression tests at room and elevated temperatures. Fig. 1 presents inverse pole figure and pole figures obtained from EBSD analysis. Its grain size ranges from 3 μm to 30 μm. This Mg alloy is strongly textured: the crystallographic *c*-axis in most grains, $\langle c\rangle$, is closely aligned with the normal direction (ND, Fig. 1). We thus refer to ND as $\langle c\rangle$ in the following discussions.

Two kinds of compression tests are conducted, for which the loading axis (LA) is either perpendicular or parallel to the *c*-axis; they are referred to as LA$\perp\langle c\rangle$ and LA$\parallel\langle c\rangle$, respectively (Fig. 2(a)). Electrical discharge machining is used to prepare cuboidal specimens as illustrated in Fig. 2(a). The sample dimensions perpendicular to the incident x-ray beam direction are 2.6 × 2.0 mm^2, and the thickness along the beam direction is 1.0 mm. For x-ray digital image correlation (XDIC), the specimens are etched with perchloric acid to produce x-ray speckles [20].

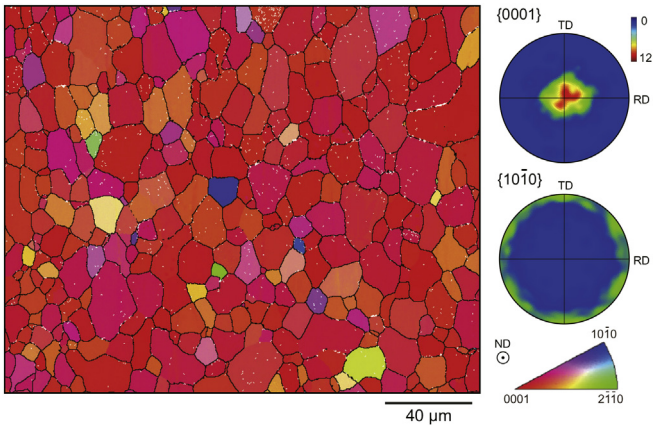

Fig. 1. Inverse pole figure map and pole figures of rolled magnesium alloy AZ31, viewed along ND. RD: rolling direction; TD: transverse direction; ND: normal direction.

Quasi-static compression tests are performed with a home-made miniature material test system (MTS) at beamline 32-ID-B of the Advanced Photon Source, which supplies highly brilliant x-rays. The experimental setup is shown in Fig. 2(b) for simultaneous, multiframe, transient x-ray diffraction [21,22] and phase contrast imaging/XDIC [20,23] measurements. To achieve μs-level temporal resolution, we use an x-ray source centered at 24.94 keV with a bandwidth of 4%. The miniature MTS (1 in Fig. 2(b)) loads a specimen (2) at room and elevated temperatures. A feedback system consisting of a thermocouple (3) and electrical heaters (4) is utilized to maintain a desired temperature. The x-rays transmitted through the sample are incident on an imaging scintillator (8), and the scattered x-rays, on a diffraction scintillator (5). Demagnifying lenses are placed after the diffraction scintillator to increase the effective reciprocal space sampled by the detector. A microchannel plate (6) is used to intensify the optical signals converted from the scattered x-rays, and synchronized with the diffraction camera (7). The recording cameras for both imaging (9) and diffraction (7) are Photron Fastcam SA-Z. The exposure times for imaging and diffraction are 1 μs and 2 μs, respectively, while their frame intervals are the same (10 μs). Similar experimental details were presented elsewhere [22,24,25].

3. Experimental results

3.1. Macroscale mechanical behavior

The true stress–strain ($\sigma-\varepsilon$) curves and corresponding strain

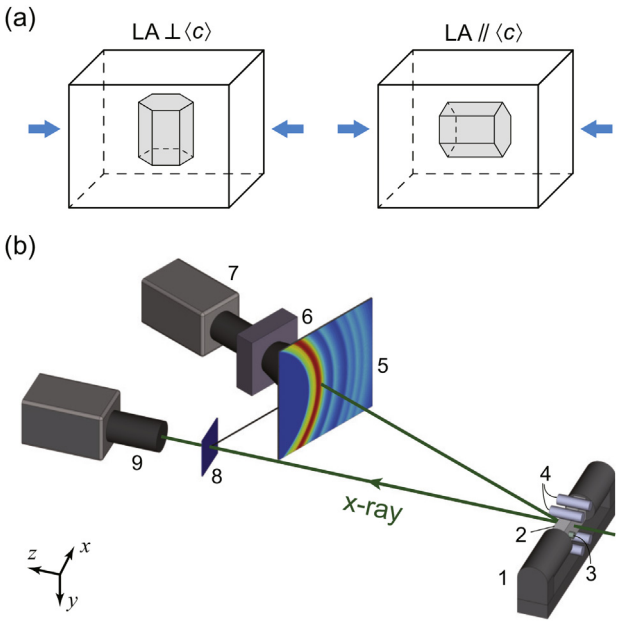

Fig. 2. (a) Illustrations of the relative orientation of the loading axis (LA) with respect to the *c*-axis. (b) Schematic of the experimental setup for simultaneous x-ray diffraction and imaging in the transmission mode under compression. The coordinate system (*xyz*) is also defined. 1: loading device (miniature MTS); 2: sample; 3: thermocouple; 4: electrical heaters; 5: diffraction scintillator (with illustrative diffraction rings of the magnesium alloy); 6: microchannel plate; 7: diffraction camera; 8: imaging scintillator; 9: imaging camera.

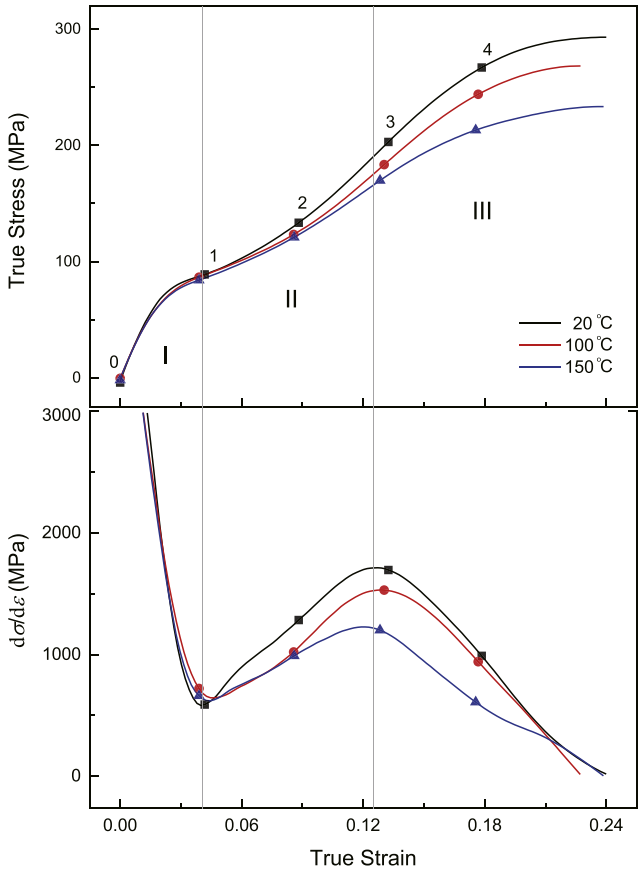

Fig. 3. Stress–strain curves and the corresponding strain hardening rate curves for the LA⊥⟨c⟩ loading at 20 °C, 100 °C and 150 °C. The symbols denote the instants for simultaneous imaging and diffraction measurements. The curves are divided into three regimes, I–III. Numbers 0–4 represent instants t_0–t_4.

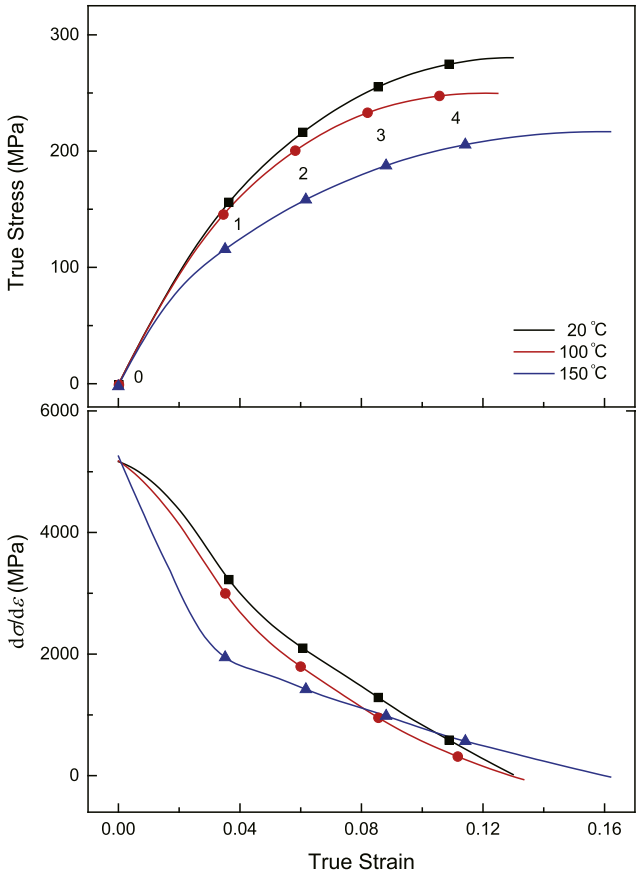

Fig. 4. Stress–strain curves and the corresponding strain hardening rate curves for the LA∥ ⟨c⟩ loading at 20 °C, 100 °C and 150 °C. The symbols denote the instants for simultaneous imaging and diffraction measurements. Numbers 0–4 represent instants t_0–t_4.

hardening rate curves for the two loading directions, LA⊥⟨c⟩ and LA∥ ⟨c⟩, are shown in Fig. 3 and Fig. 4, respectively, for three different temperatures (20 °C, 100 °C and 150 °C). The strain rate is approximately 10^{-3} s^{-1}. In the LA⊥⟨c⟩ case, the $\sigma - \varepsilon$ curves for all test temperatures exhibit sigmoidal shapes, while those for the LA∥ ⟨c⟩ loading are concave downward. Moreover, the strain hardening rates for the LA∥ ⟨c⟩ loading decrease monotonically. In contrast, the strain hardening rate versus true strain ($d\sigma/\ d\varepsilon - \varepsilon$) curves for the LA⊥⟨c⟩ loading demonstrate three regimes: the strain hardening rate decreases rapidly upon initial yield, as expected for an elastic–plastic transition (regime I); the rate then experiences a distinct increase followed by a sharp decrease (regimes II and III, respectively). In addition, with increasing temperature, the flow stresses of both LA⊥⟨c⟩ and LA∥ ⟨c⟩ loading reduce significantly, and the strain hardening rates decrease as well.

3.2. Mesoscale strain field measurements

During quasi-static compression tests at different temperatures, image sequences are acquired via synchrotron x-ray phase contrast imaging [23]. To understand mesoscale deformation, the image sequences are used to map the strain fields with XDIC [20]. The XDIC method resorts to uniformly distributed x-ray speckles which are originated from micron-scale surface roughness or internal isolated structure features, and "traces" the speckles in x-ray images to resolve displacements via image correlation between two adjacent frames. The Green-Lagrange normal strains (E_{xx}) is calculated from displacement (u) gradients as

$$E_{ij} = \frac{1}{2}\left(u_{i,j} + u_{j,i} + u_{k,i}u_{k,j}\right), \tag{1}$$

where $i, j, k = x, y$.

The normal strain fields, $E_{xx}(x, y)$, for the LA⊥⟨c⟩ and LA∥ ⟨c⟩ loading obtained at instants noted in Figs. 3 and 4, are shown in Fig. 5. The areas with poor correlation are replaced with white pixels. At room temperature, the LA⊥⟨c⟩ sample show relatively homogeneous deformation (t_2, t_3) after the elastic–plastic transition (t_1), and then an obvious accumulation of localized plastic strain (t_4), while the normal strain field maps (E_{xx}) for the LA∥ ⟨c⟩ loading experiences continuous local deformation accumulation (t_1–t_4). Strain field evolutions with increasing strain at evaluated temperatures (100 °C and 150 °C) are similar to those at the room temperature, in both LA⊥⟨c⟩ and LA∥ ⟨c⟩ cases.

In order to quantify the effect of temperature on strain field evolution, the degrees of inhomogeneity of normal strain fields as a function of true strain at different temperatures are calculated (Fig. 6). The degree of inhomogeneity ($\mathcal{C}$), or the coefficient of spatial variation of E_{xx}, is defined as

$$\mathcal{C} = \frac{\mathrm{Stdev}(E_{xx})}{\mathrm{Avg}(E_{xx})}, \tag{2}$$

where Stdev and Avg are standard deviation and spatial average of normal strain, respectively. The degrees of inhomogeneity for each

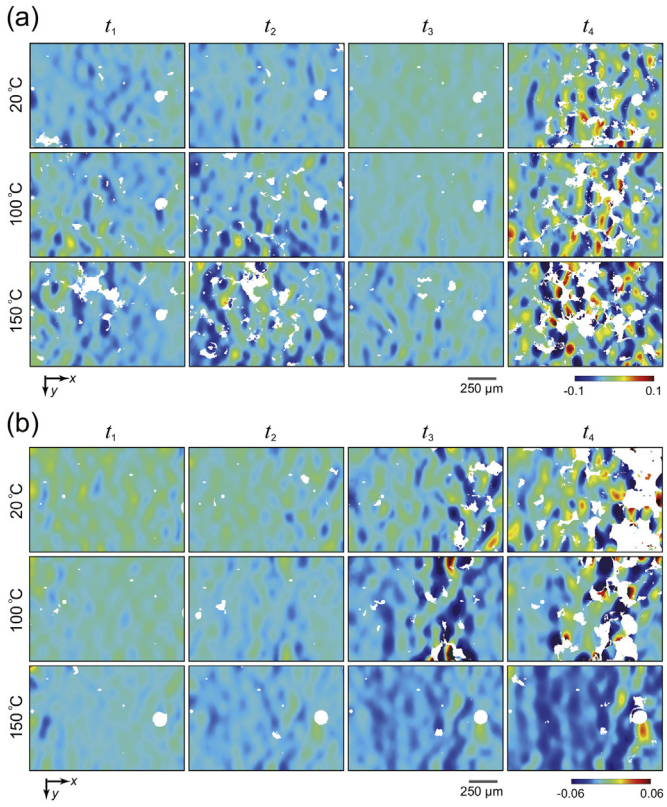

Fig. 5. Green-Lagrange normal strain field maps (E_{xx}) at instants t_1–t_4 obtained from XDIC for the LA⊥⟨c⟩ (a) and LA∥ ⟨c⟩ (b) loading at different temperatures.

loading direction at different temperatures exhibit similar trends, which are consistent with strain fields evolution (Fig. 5). With increasing temperature, $\mathcal{C}$ for the LA⊥⟨c⟩ loading increases slight slightly, while it decreases for the LA∥ ⟨c⟩ loading.

3.3. Microscale x-ray diffraction measurements

In addition to phase contrast imaging and stress–strain curves, two-dimensional x-ray diffraction patterns are acquired simultaneously. The diffraction rings as shown in Fig. 7(a) are indexed and converted to one-dimensional diffraction curves (intensity versus 2θ) via azimuthal integral with the HiSPoD program [26]. Here θ is the scattering angle. Fig. 7(b) shows the integrated diffraction curves of undeformed LA⊥⟨c⟩ and LA∥ ⟨c⟩ samples at different temperatures, and temperature appears to have negligible effects on the diffraction patterns at zero applied stress. Consistent with the pole figures of the as-received sample (Fig. 1), there are initially no diffracted x-rays from the basal planes, {0002}, from the undeformed LA⊥⟨c⟩ samples, but their diffraction peaks from the prismatic planes, $\{10\bar{1}0\}$ and $\{11\bar{2}0\}$, are strong. In contrast, the {0002} reflection dominates the $\{10\bar{1}0\}$ and $\{11\bar{2}0\}$) reflections for the undeformed LA∥ ⟨c⟩ samples, given the initial texture.

Similar to the deformation at room temperature, the {0002} reflections experience significant changes as deformation proceeds at elevated temperatures. The {0002} peak intensities as a function of true strain are shown in Fig. 8 for the LA⊥⟨c⟩ and LA∥ ⟨c⟩ samples at 20 °C, 100 °C and 150 °C. A previous study demonstrated that the {0002} peak intensity is augmented by $\{10\bar{1}2\}$ extension twinning ($\sim 90^\circ$ re-orientation) but reduced by dislocation motion [14]. As plastic deformation proceeds at a given temperature, all the {0002} reflections of the LA⊥⟨c⟩ samples undergo a pronounced growth;

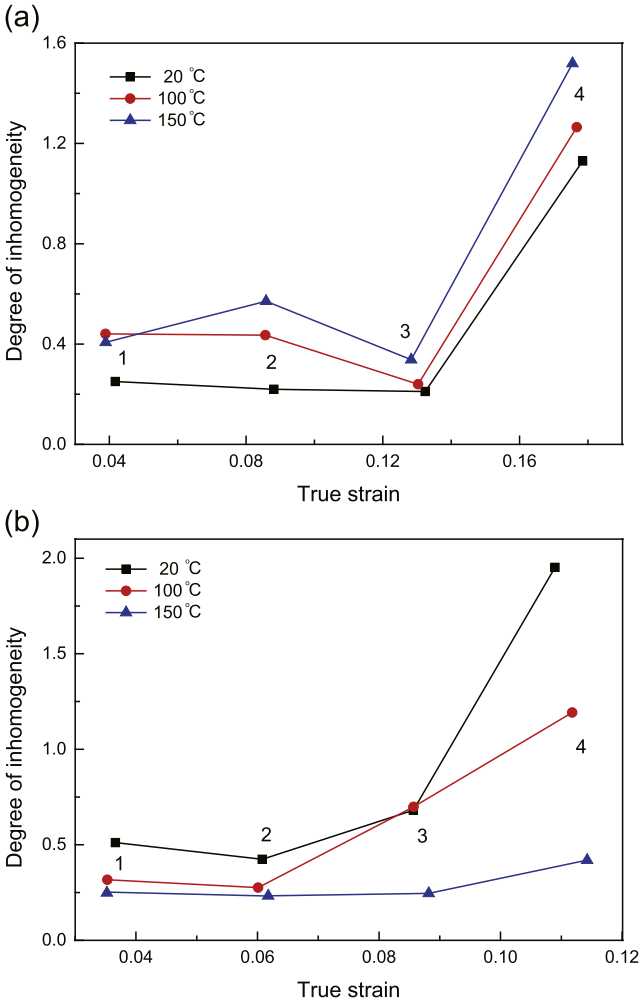

Fig. 6. Degrees of inhomogeneity of normal strain fields as a function of true strain for the LA⊥⟨c⟩ (a) and LA∥ ⟨c⟩ (b) loading at different temperatures.

the intensities at the same strain decrease with increasing temperature. It can be inferred that the $\{10\bar{1}2\}$ extension twinning dominates the deformation for the LA⊥⟨c⟩ loading, and fewer twins are activated at elevated temperatures. Nevertheless, for the LA∥ ⟨c⟩ loading, few twins are activated, and the plastic deformation is mainly achieved by dislocation motion, since the {0002} peak intensities increase slightly to a similar plateau (for different temperatures) and then decrease with increasing strain. Moreover, the reduction in the {0002} peak intensity occurs at a smaller strain for a higher temperature, indicating that fewer defects are activated at elevated temperatures.

4. Discussions

The main deformation modes in magnesium alloy AZ31 under quasi-static loading include four slip modes and one twinning mode (Fig. 9): basal ⟨a⟩, $\{0001\}\langle 11\bar{2}0\rangle$ [1]; prismatic ⟨a⟩, $\{1\bar{1}00\}\langle 11\bar{2}0\rangle$; pyramidal ⟨$a$⟩, $\{1\bar{1}01\}\langle 11\bar{2}0\rangle$; pyramidal ⟨$c+a$⟩, $\{11\bar{2}2\}\langle\bar{1}\bar{1}23\rangle$; and extension twinning, $\{10\bar{1}2\}\langle\bar{1}011\rangle$. Among these modes, pyramidal ⟨$c+a$⟩ slip is the only slip mode accommodating deformation along the c-axis, while the other slip modes can only provide deformation within basal planes. $\{10\bar{1}2\}$ extension twinning can also accommodate deformation along the crystal c-axis.

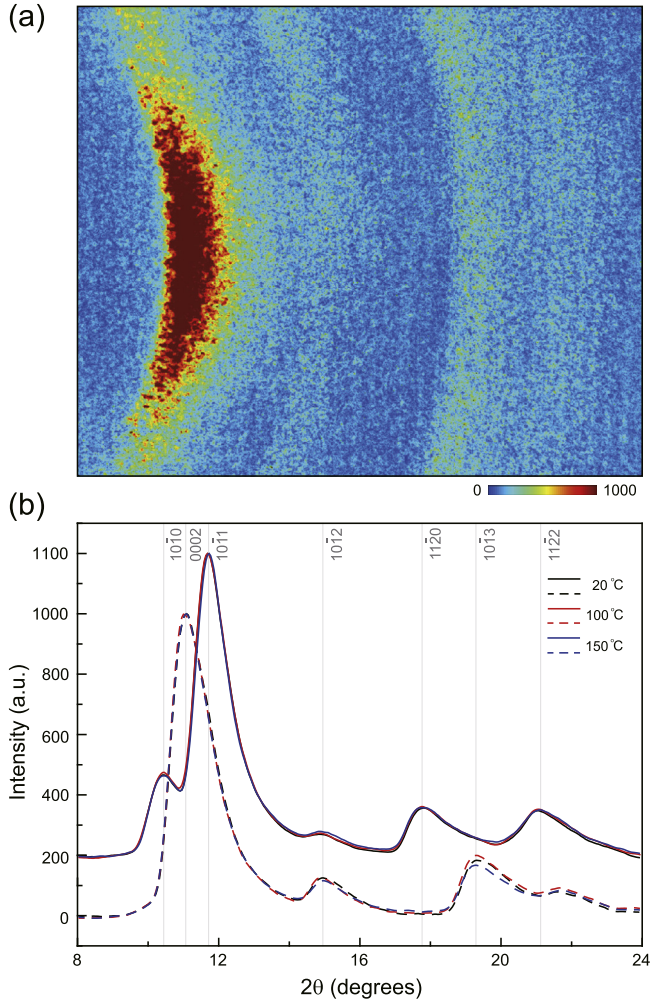

Fig. 7. (a) Two-dimensional diffraction pattern of the undeformed LA‖ ⟨*c*⟩ sample at room temperature. (b) X-ray diffraction peak patterns of the undeformed samples at different temperatures for the LA⊥⟨*c*⟩ (solid curves) and LA‖ ⟨*c*⟩ (dash curves) loading. The baselines are shifted for clarity.

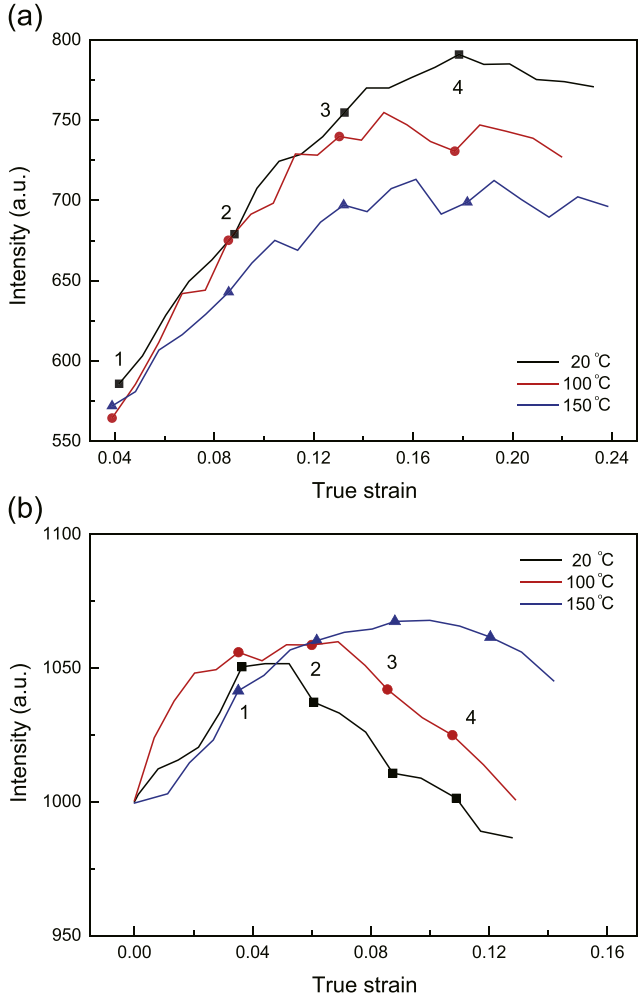

Fig. 8. X-ray diffraction peak intensities of {0002} reflections at instants t_0–t_4 for the LA⊥⟨*c*⟩ (a) and LA‖ ⟨*c*⟩ (b) loading at different temperatures.

During compression, deformation perpendicular to LA is indispensable due to the Poisson effect, besides that along LA. At room temperature, abundant $\{10\bar{1}2\}$ extension twins are activated for the LA⊥⟨*c*⟩ loading, to accommodate the deformation perpendicular to LA in regime II, resulting in homogenization of plastic deformation as manifested in strain fields (lower C values, Fig. 6(a)), and the pronounced increase in strain hardening rate. On the other hand, for the LA‖ ⟨*c*⟩ loading, the pyramidal ⟨$c+a$⟩ slip dominates the deformation along the crystallographic *c*-axis. At low bulk stress levels, the pyramidal ⟨$c+a$⟩ slip can only be activated in the stress concentration region to accommodate the deformation along LA, because of high CRSS at room temperature. Consequently, the mesoscale strain fields show inhomogeneous plastic deformation and the corresponding macroscopic mechanical behavior exhibits a decrease in strain hardening rate.

With increasing temperature, CRSS of basal ⟨*a*⟩ slip varies slightly, but those for prismatic ⟨*a*⟩ slip and pyramidal ⟨$c+a$⟩ slip decrease substantially. On the contrary, twin nucleation is not thermally activated but rather occurs at high stress concentrations [27]. At elevated temperatures, because of the initial texture, extension twinning still dominates the deformation along the *c*-axis for the LA⊥⟨*c*⟩ loading. However, fewer stress concentration places are observed in the LA⊥⟨*c*⟩ samples due to readily activated dislocation slips, and the number of $\{10\bar{1}2\}$ extension twins undergoes a certain reduction. The decreases in {0002} peak intensities confirm this. Moreover, the decrease in number of twins

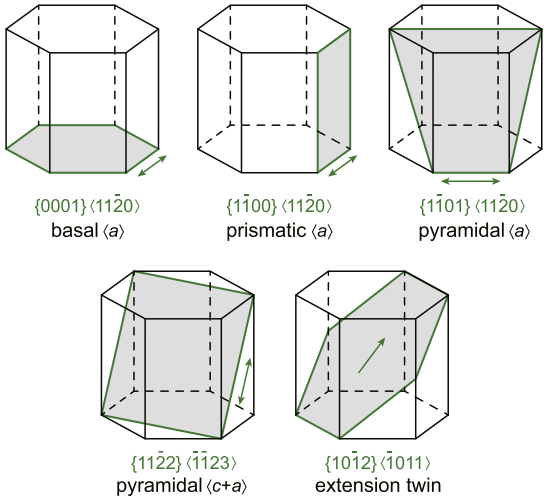

Fig. 9. Schematic illustrations of main deformation modes in magnesium alloy. The double-headed arrows indicate slip, while the single-headed arrow marks the polarity of twinning.

gives rise to higher $\mathcal{C}$ values, and increased inhomogeneity at higher temperatures slows down the increase in strain hardening rate in regime II. For the LA$\|\langle c\rangle$ loading, the pyramidal $\langle c+a\rangle$ slip at elevated temperatures (100 °C and 150 °C) can be activated more uniformly to accommodate the deformation along *c*-axis, resulting in decrease in $\mathcal{C}$. In addition, the homogenization of plastic deformation slows down the reduction of strain hardening rate.

Regarding the effects of loading direction and temperature on deformation of AZ31, it can be inferred that both pyramidal $\langle c+a\rangle$ dislocation slip at elevated temperatures and $\{10\bar{1}2\}$ extension twinning at low temperatures can result in more homogeneous plastic deformation by accommodating the deformation along and perpendicular to LA, and the homogenization can accelerate the increase or slow down the decrease of strain hardening rate during the early stage of plastic deformation (t_1–t_3, Fig. 8). Moreover, at a given temperature (20 °C, 100 °C or 150 °C), $\{10\bar{1}2\}$ extension twinning induces homogeneous deformation with increasing strain, and a reduction in strain localization effectively boosts macroscale strain hardening rate for the LA$\perp\langle c\rangle$ loading. On the other hand, dislocation motion leads to continuous local deformation accumulation in the LA$\|\langle c\rangle$ samples, and mesoscale inhomogeneous deformation induces reduced strain hardening rate.

5. Conclusions

A textured magnesium alloy AZ31 is compressed uniaxially with LA$\perp\langle c\rangle$ or LA$\|\langle c\rangle$ at different temperatures in conjunction with *in situ* synchrotron x-ray imaging and diffraction. Simultaneous multiscale measurements are obtained in terms of true stress–strain curves (macroscale), normal strain fields (mesoscale) and diffraction patterns (microscale). The current work differs from previous studies in its added mesoscale measurements which bridge macro- and microscales. Our main conclusions are as follows.

- The stress–strain curves and corresponding strain hardening rates show strong anisotropy due to the initial texture.
- With increasing temperature, fewer $\{10\bar{1}2\}$ extension twins are activated in the LA$\perp\langle c\rangle$ samples, giving rise to reduced strain homogenization, while pyramidal $\langle c+a\rangle$ slip becomes readily activated, leading to more homogeneous deformation for the LA$\|\langle c\rangle$ loading.
- With increasing strain, the reduction in strain localizations boosts effectively strain hardening rate, while strain concentrations induce reduced strain hardening rate.
- Both pyramidal $\langle c+a\rangle$ dislocation slip and $\{10\bar{1}2\}$ extension twinning can result in homogenization in plastic deformation by accommodating the deformation along and perpendicular to the crystallographic *c*-axis.

Acknowledgments

We thank A. Deriy and Dr. J. Wang at the APS, and the PIMS x-ray team for the experimental support. The AZ31 samples were supplied by Dr. F. Zhao at PIMS. This work was sponsored in part by the 973 project of China (No. 2014CB845904), and NSFC (Nos. 11627901 and 11672254). Use of the Advanced Photon Source, an Office of Science User Facility operated for the U.S. Department of Energy (DOE) Office of Science by Argonne National Laboratory, was supported by the U.S. DOE under Contract No. DE-AC02-06CH11357.

References

[1] C.S. Roberts, Magnesium and its Alloys, Wiley, New York, 1960.
[2] T. Obara, H. Yoshinga, S. Morozumi, $\{11\bar{2}2\}\langle 1123\rangle$ slip system in magnesium, Acta Metall. 21 (1973) 845–853.
[3] X.Y. Lou, M. Li, R.K. Boger, S.R. Agnew, R.H. Wagoner, Hardening evolution of AZ31B Mg sheet, Int. J. Plast. 23 (2007) 44–86.
[4] J.F. Stohr, J.P. Poirier, Etude en microscopie electronique du glissement pyramidal $\{1122\}\langle 1123\rangle$ dans le magnesium, Philos. Magn. 25 (1972) 1313–1329.
[5] Z. Keshavarz, M.R. Barnett, EBSD analysis of deformation modes in Mg–3Al–1Zn, Scr. Mater. 55 (2006) 915–918.
[6] O. Muránsky, D.G. Carr, M.R. Barnett, E.C. Oliver, P. Šittner, Investigation of deformation mechanisms involved in the plasticity of AZ31 Mg alloy: in situ neutron diffraction and EPSC modelling, Mater. Sci. Eng. A 496 (2008) 14–24.
[7] M. Yoo, Slip, twinning, and fracture in hexagonal close-packed metals, Metall. Trans. A 12 (1981) 409–418.
[8] N.V. Dudamell, I. Ulacia, F. Gálvez, S. Yi, J. Bohlen, D. Letzig, I. Hurtado, M.T. Pérez-Prado, Twinning and grain subdivision during dynamic deformation of a Mg AZ31 sheet alloy at room temperature, Acta Mater. 59 (2011) 6949–6962.
[9] N. Stanford, M. Barnett, Effect of composition on the texture and deformation behaviour of wrought Mg alloys, Scr. Mater. 58 (2008) 179–182.
[10] M. Wang, L. Lu, C. Li, X.H. Xiao, X.M. Zhou, J. Zhu, S.N. Luo, Deformation and spallation of a magnesium alloy under high strain rate loading, Mater. Sci. Eng. A 661 (2016) 126–131.
[11] K. Hazeli, J. Cuadra, P. Vanniamparambil, A. Kontsos, In situ identification of twin-related bands near yielding in a magnesium alloy, Scr. Mater. 68 (1) (2013) 83–86.
[12] J. Kang, D.S. Wilkinson, R.K. Mishra, W. Yuan, R.S. Mishra, Effect of inhomogeneous deformation on anisotropy of AZ31 magnesium sheet, Mater. Sci. Eng. A 567 (2013) 101–109.
[13] C.C. Aydıner, M.A. Telemez, Multiscale deformation heterogeneity in twinning magnesium investigated with *in situ* image correlation, Int. J. Plast. 56 (2014) 203–218.
[14] L. Lu, J.W. Huang, D. Fan, B.X. Bie, T. Sun, K. Fezzaa, X.L. Gong, S.N. Luo, Anisotropic deformation of extruded magnesium alloy AZ31 under uniaxial compression: a study with simultaneous in situ synchrotron x-ray imaging and diffraction, Acta Mater. 120 (2016) 86–94.
[15] F.-K. Chen, T.-B. Huang, Formability of stamping magnesium-alloy AZ31 sheets, J. Mater. Process. Technol. 142 (3) (2003) 643–647.
[16] Y. Lee, M. Kim, S. Kim, Y. Kwon, S. Choi, J. Lee, Experimental and analytical studies for forming limit of AZ31 alloy on warm sheet metal forming, J. Mater. Process. Technol. 187 (2007) 103–107.
[17] A. Jain, S.R. Agnew, Modeling the temperature dependent effect of twinning on the behavior of magnesium alloy AZ31B sheet, Mater. Sci. Eng. A 462 (2007) 29–36.
[18] A. Khosravani, J. Scott, M. Miles, D. Fullwood, B. Adams, R. Mishra, Twinning in magnesium alloy AZ31B under different strain paths at moderately elevated temperatures, Int. J. Plast. 45 (2013) 160–173.
[19] A. Chapuis, J.H. Driver, Temperature dependency of slip and twinning in plane strain compressed magnesium single crystals, Acta Mater. 59 (2011) 1986–1994.
[20] L. Lu, D. Fan, B.X. Bie, X.X. Ran, M.L. Qi, N. Parab, J.Z. Sun, H.J. Liao, M.C. Hudspeth, B. Claus, K. Fezzaa, T. Sun, W. Chen, X.L. Gong, S.N. Luo, Note: dynamic strain field mapping with synchrotron X-ray digital image correlation, Rev. Sci. Instrum. 85 (2014) 076101.
[21] P. Lambert, C. Hustedt, K. Vecchio, E. Huskins, D. Casem, S. Gruner, M. Tate, H. Philipp, A. Woll, P. Purohit, J. Weiss, V. Kannan, K. Ramesh, P. Kenesei, J. Okasinski, J. Almer, M. Zhao, A. Ananiadis, T. Hufnagel, Time-resolved x-ray diffraction techniques for bulk polycrystalline materials under dynamic loading, Rev. Sci. Instrum. 85 (2014) 093901.
[22] D. Fan, L. Lu, B. Li, M.L. Qi, J.C. E, F. Zhao, T. Sun, K. Fezzaa, W. Chen, S.N. Luo, Transient x-ray diffraction with simultaneous imaging under high strain-rate loading, Rev. Sci. Instrum. 85 (2014) 113902.
[23] M. Hudspeth, B. Claus, S. Dubelman, J. Black, A. Mondal, N. Parab, C. Funnell, F. Hai, M.L. Qi, K. Fezzaa, S.N. Luo, W. Chen, High speed synchrotron x-ray phase contrast imaging of dynamic material response to split Hopkinson bar loading, Rev. Sci. Instrum. 84 (2013) 025102.
[24] B.X. Bie, J.Y. Huang, B. Su, L. Lu, D. Fan, J.C. E, T. Sun, K. Fezzaa, M.L. Qi, S.N. Luo, Dynamic tensile deformation and damage of B_4 C-reinforced Al composites: time-resolved imaging with synchrotron x-rays, Mater. Sci. Eng. A 664 (2016) 86–93.
[25] J.Y. Huang, J.C. E, J.W. Huang, T. Sun, K. Fezzaa, S.L. Xu, S.N. Luo, Dynamic deformation and fracture of single crystal silicon: fracture modes, damage laws, and anisotropy, Acta Mater. 114 (2016) 136–145.
[26] T. Sun, K. Fezzaa, HiSPoD: a program for high-speed polychromatic x-ray diffraction experiments and data analysis on polycrystalline sample, J. Synchrotron Radiat. 23 (2016) 1046–1053.
[27] J.W. Christian, S. Mahajan, Deformation twinning, Prog. Mater. Sci. 39 (1995) 1–157.